

# An Evolutionary Optimization Method for Solving the Multi-Frequency GPR Subsurface Problem

M. Salucci, L. Poli, N. Anselmi, and A. Massa

## Abstract

In this work, the two-dimensional subsurface imaging problem is solved by processing wide-band ground penetrating radar (*GPR*) data. Towards this end, an innovative microwave inverse scattering technique is presented. The developed methodology is based on a particle swarm optimization (*PSO*) solver to minimize the arising multi-frequency (*MF*) cost function measuring the mismatch between measured and retrieved data. Moreover, an iterative multi-resolution strategy is exploited in order to progressively and adaptively refine the resolution of the retrieved images only within the regions of interest in which the presence of a buried object has been detected. Some numerical results are shown, in order to assess the effectiveness of the developed *MF-IMSA-PSO* strategy in reconstructing dielectric objects buried at different depths. Some experiments are also shown to verify the robustness of the proposed method when the background permittivity is not constant but smoothly varying with the distance from the interface.

# 1 Definitions

## 1.1 Glossary

- $SF$ : Single-Frequency;
- $FH$ : Frequency-Hopping;
- $MF$ : Multi-Frequency;
- $P$ : Swarm dimension;
- $U$ : Total number of unknowns;
- $S$ : Maximum number of  $IMSA$  zooming steps;
- $s^{best}$ : Last performed  $IMSA$  zooming step ( $s^{best} \leq S$ );
- $\eta_{th}$ :  $IMSA$  zooming threshold;
- $D_{inv}$ : Investigation domain;
- $D_{obs}$ : Observation domain;
- $L$ : Side of the investigation domain;
- $N$ : Number of discretization cells in  $D_{inv}$ ;
- $V$ : Number of views;
- $M$ : Number of measurement points;
- $F$ : Number of frequencies considered for the inversion;
- $\mathbf{r}^{(v)} = (x^{(v)}, y^{(v)})$ : Coordinates of the  $v$ -th source ( $v = 1, \dots, V$ ).
- $\mathbf{r}_m^{(v)} = (x_m^{(v)}, y_m^{(v)})$ : Coordinates of the  $m$ -th measurement point for the  $v$ -th view  $v$ , ( $m = 1, \dots, M$ );
- $\varepsilon_{ra} = \frac{\varepsilon_a}{\varepsilon_0}$ : Relative electric permittivity for the upper half-space ( $y > 0$ );
- $\sigma_a$ : Conductivity for the upper half-space ( $y > 0$ );
- $\varepsilon_{rb} = \frac{\varepsilon_b}{\varepsilon_0}$ : Background relative electric permittivity;
- $\sigma_b$ : Background conductivity;
- $E_{inc}^{(v)}(\mathbf{r}_n; f)$ : Measured internal incident field inside the  $n$ -th cell, for the  $v$ -th view at frequency  $f$ ;
- $\tilde{E}_{inc}^{(v)}(\mathbf{r}_n; f)$ : Computed internal incident field inside the  $n$ -th cell, for the  $v$ -th view at frequency  $f$ ;
- $E_{scatt}^{(v)}(\mathbf{r}_m^{(v)}; f)$ : Measured external scattered by the  $m$ -th measurement point, for the  $v$ -th view at frequency  $f$ ;
- $\tilde{E}_{scatt}^{(v)}(\mathbf{r}_m^{(v)}; f)$ : Measured external scattered by the  $m$ -th measurement point, for the  $v$ -th view at frequency  $f$ .

## 1.2 Contrast function

The contrast function at frequency  $f$  is defined as

$$\tau(\mathbf{r}; f) = \frac{\varepsilon_{eq}(\mathbf{r}) - \varepsilon_{eqb}}{\varepsilon_0} = [\varepsilon_r(\mathbf{r}) - \varepsilon_{rb}] + j \left[ \frac{\sigma_b - \sigma(\mathbf{r})}{2\pi f \varepsilon_0} \right]$$

where

- $\mathbf{r} = (x, y)$ : position vector;
- $\Re\{\tau(\mathbf{r}; f)\} = [\varepsilon_r(\mathbf{r}) - \varepsilon_{rb}]$  ;
- $\Im\{\tau(\mathbf{r}; f)\} = \left[ \frac{\sigma_b - \sigma(\mathbf{r})}{2\pi f \varepsilon_0} \right]$  ;
- $\varepsilon_{eq}(\mathbf{r}) = \varepsilon_0 \varepsilon_r(\mathbf{r}) - j \frac{\sigma(\mathbf{r})}{2\pi f}$  ;
- $\varepsilon_{eqb} = \varepsilon_0 \varepsilon_{rb} - j \frac{\sigma_b}{2\pi f}$  ;
- $\varepsilon_r(\mathbf{r})$ : relative electric permittivity at position  $\mathbf{r}$  ;
- $\sigma(\mathbf{r})$ : conductivity at position  $\mathbf{r}$  ;

**NOTE:** we assume that  $\varepsilon_r(\mathbf{r})$  and  $\sigma(\mathbf{r})$  are **not frequency dependent** (non-dispersive mediums).

### 1.2.1 Contrast function and reference frequency $f_{ref}$ (MF approaches)

The contrast function at a generic frequency  $f$  can be expressed by means of the contrast function computed for a selected reference frequency

$$f = f_{ref} \tag{1}$$

as follows

$$\tau(\mathbf{r}; f) = \Re\{\tau(\mathbf{r}; f_{ref})\} + j \frac{f_{ref}}{f} \Im\{\tau(\mathbf{r}; f_{ref})\}. \tag{2}$$

This allows to reduce the number of unknowns when dealing with multi-frequency techniques, since we can just consider the contrast function at the reference frequency.

### 1.3 Cost function & unknowns

#### 1.3.1 Multi-Frequency ( $MF$ ) approaches

These approaches jointly consider data at  $F$  frequencies. The functional minimized by the inversion algorithm is defined as

$$\Phi(\mathbf{x}) = \Phi_{state}(\mathbf{x}) + \Phi_{data}(\mathbf{x}) \quad (3)$$

where  $\Phi_{state}(\mathbf{x})$  and  $\Phi_{data}(\mathbf{x})$  are respectively the data and state terms of the cost function, defined as

$$\Phi_{state}(\mathbf{x}) = \frac{\sum_{j=1}^F \sum_{v=1}^V \sum_{n=1}^N |E_{inc}^{(v)}(\mathbf{r}_n; f_j) - \tilde{E}_{inc}^{(v)}(\mathbf{r}_n; f_j)|^2}{\sum_{j=1}^F \sum_{v=1}^V \sum_{n=1}^N |E_{inc}^{(v)}(\mathbf{r}_n; f_j)|^2} \quad (4)$$

$$\Phi_{data} = \frac{\sum_{j=1}^F \sum_{v=1}^V \sum_{m=1}^M |E_{scatt}^{(v)}(\mathbf{r}_m^{(v)}; f_j) - \tilde{E}_{scatt}^{(v)}(\mathbf{r}_m^{(v)}; f_j)|^2}{\sum_{j=1}^F \sum_{v=1}^V \sum_{m=1}^M |E_{scatt}^{(v)}(\mathbf{r}_m^{(v)}; f_j)|^2} \quad (5)$$

The unknowns of the inversion problem are

$$\mathbf{x} = \left\{ \tau(\mathbf{r}; f_{ref}); E_{tot}^{(v)}(\mathbf{r}_n; f_j) \right\} \quad n = 1, \dots, N; v = 1, \dots, V; j = 1, \dots, F. \quad (6)$$

The total number of unknowns for  $MF$ -based approaches is then given by

$$U_{MF} = 2N(1 + VF). \quad (7)$$

### 1.4 Reconstruction errors

The following integral error is defined

$$\Xi_{reg} = \frac{1}{N_{reg}} \sum_{n=1}^{N_{reg}} \frac{|\tau_n^{act} - \tau_n^{rec}|}{|\tau_n^{act} + 1|} \quad (8)$$

where  $reg$  indicates if the error computation covers

- the overall investigation domain ( $reg \Rightarrow tot$ ),
- the actual scatterer support ( $reg \Rightarrow int$ ),
- or the background region ( $reg \Rightarrow ext$ ).

## 2 Variation of the object depth

### 2.1 Circular object ( $\varepsilon_{r,obj} = 5.0$ , $\sigma_{obj} = 10^{-3}$ [S/m])

#### 2.1.1 Parameters

##### Background

Inhomogeneous and nonmagnetic background composed by two half spaces

- Upper half space ( $y > 0$  - air):  $\varepsilon_{ra} = 1.0$ ,  $\sigma_a = 0.0$ ;
- Lower half space ( $y < 0$  - soil):  $\varepsilon_{rb} = 4.0$ ,  $\sigma_b = 10^{-3}$ [S/m];

##### Investigation domain ( $D_{inv}$ )

- Side:  $L_{D_{inv}} = 0.8$  [m];
- Barycenter:  $(x_{bar}^{D_{inv}}, y_{bar}^{D_{inv}}) = (0.00, -0.4)$  [m];

##### Time-Domain forward solver ( $FDTD - GPRMax2D$ )

- Side of the simulated domain:  $L = 6$  [m];
- Number of cells:  $N^{FDTD} = 750 \times 750 = 5.625 \times 10^5$ ;
- Side of the  $FDTD$  cells  $l^{FDTD} = 0.008$  [m];
- Simulation time window:  $T^{FDTD} = 20 \times 10^{-9}$  [sec];
- Time step:  $\Delta t^{FDTD} = 1.89 \times 10^{-11}$  [sec];
- Number of time samples:  $N_t^{FDTD} = 1060$ ;
- Boundary conditions: perfectly matched layer ( $PML$ );
- Source type: Gaussian mono-cycle (first Gaussian pulse derivative, called "Ricker" in  $GPRMax2D$ )
  - Central frequency:  $f_0 = 300$  [MHz];
  - Source amplitude:  $A = 1.0$  [A];

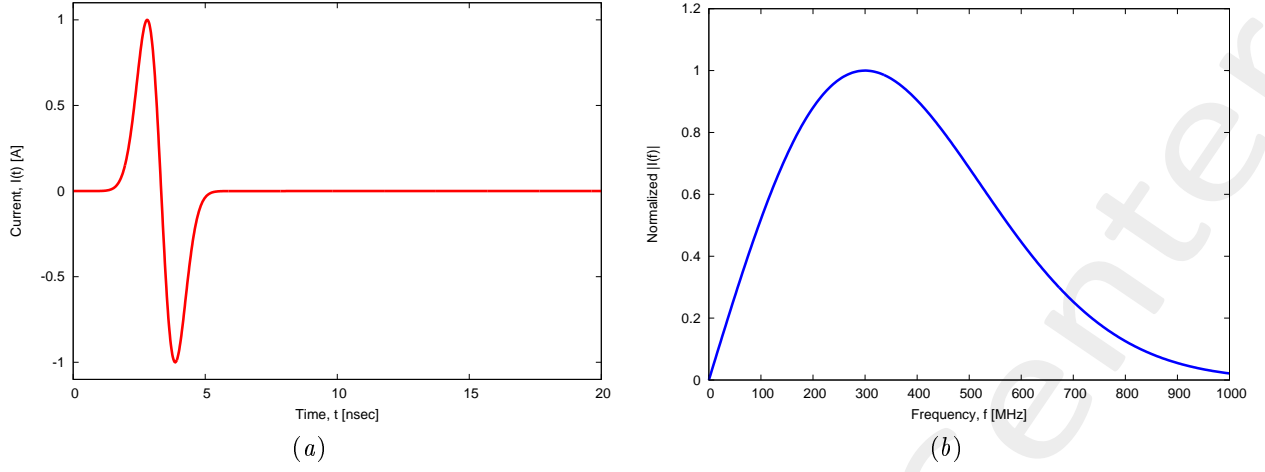


Figure 1: *GPRMax2D* excitation signal. (a) Time pulse, (b) normalized frequency spectrum.

### Frequency parameters

- Frequency range:  $f \in [f_{min}, f_{max}] = [200.0, 600.0]$  [MHz] ( $-3$  [dB] bandwidth of the Gaussian Monocycle excitation centered at  $f_0 = 300$  [MHz]);
- Frequency step:  $\Delta f = 100$  [MHz] ( $F = 5$  frequency steps in  $[f_{min}, f_{max}]$ );

$f$ [MHz]	$\lambda_a$ [m]	$\lambda_b$ [m]	$f^*$ [MHz]
200.0	1.50	0.75	200.5
300.0	1.00	0.50	297.6
400.0	0.75	0.37	401.1
500.0	0.60	0.30	498.1
600.0	0.50	0.25	601.6

Table 1: Considered frequencies and corresponding wavelength in the upper medium ( $\lambda_a$ , free space) and in the lower medium ( $\lambda_b$ , soil).  $f^*$  is the nearest frequency sample available from transformed time-domain data, and represents the real frequency considered by the inversion algorithm.

### Scatterer

- Type: Circular;
- Barycenter:
  - **Case 1:**  $d_{obj} = 0.16$  [m]  $\rightarrow (x_{obj}, y_{obj}) = (0.0, -0.16)$  [m];
  - **Case 2:**  $d_{obj} = 0.4$  [m]  $\rightarrow (x_{obj}, y_{obj}) = (0.0, -0.4)$  [m];
  - **Case 3:**  $d_{obj} = 0.64$  [m]  $\rightarrow (x_{obj}, y_{obj}) = (0.0, -0.64)$  [m];
- Radius:  $r_{obj} = 0.08$  [m];
- Electromagnetic properties:  $\varepsilon_{r,obj} = 5.0$ ,  $\sigma_{obj} = 10^{-3}$  [S/m] ( $\sigma_{obj} = \sigma_b$ );
- Contrast function:  $\tau = 1.0 + j0.0$

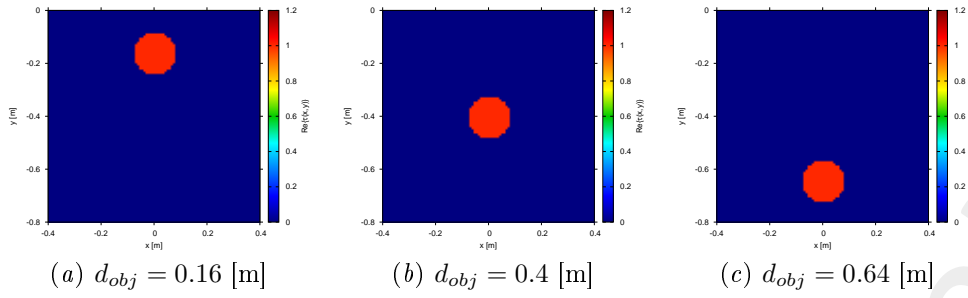


Figure 2: Actual object.

### Measurement setup

- Considered frequency:  $f_{min} = 200$  [MHz],  $\lambda_b = 0.75$  [m].<sup>1</sup>
- #DoFs =  $2ka = \frac{2\pi}{\lambda_b} L\sqrt{2} = \frac{2\pi}{0.75} 0.8\sqrt{2} \simeq 9.5$ ;
- Number of views (sources):  $V = 10$ ;
  - $\min\{x_v\} = -0.5$  [m],  $\max\{x_v\} = 0.5$  [m];
  - height:  $y_v = 0.1$  [m],  $\forall v = 1, \dots, V$ ;
- Number of measurement points:  $M = 9$ ;
  - $\min\{x_m\} = -0.5$  [m],  $\max\{x_m\} = 0.5$  [m];
  - height:  $y_m = 0.1$  [m],  $\forall m = 1, \dots, M$ ;

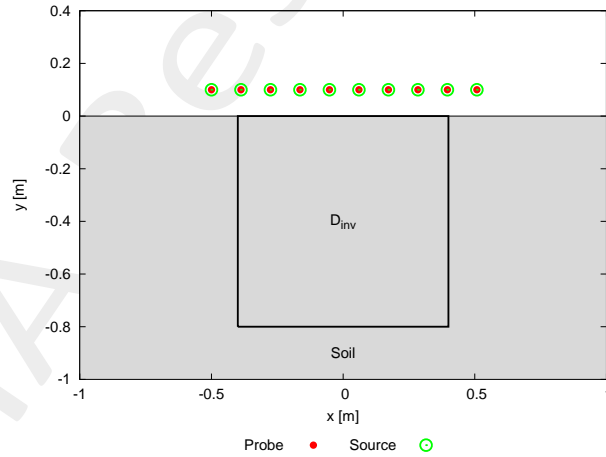


Figure 3: Location of the measurement points ( $M = 9$ ) and of the sources ( $V = 10$ ). Only one source is active for each view.

### Inverse solver parameters

- Shared parameters
  - Number of unknowns:  $U = 2N(1 + VF) = 4998$ ;

<sup>1</sup>NOTE: This choice is done in order to keep the number of unknowns lower than 5000.

- Weight of the state term of the functional: 1.0;
- Weight of the data term of the functional: 1.0;
- Weight of the penalty term of the functional: 0.0;
- Convergence threshold:  $10^{-10}$ ;
- Variable ranges:
  - \*  $\varepsilon_r \in [4.0, 5.2]$ ;
  - \*  $\sigma \in [8.0 \times 10^{-4}, 1.2 \times 10^{-3}]$  [S/m];
  - \*  $\Re \{E_{tot}^{int}\} \in [-8, 8]$ ,  $\Im \{E_{tot}^{int}\} \in [-8, 8]$ ;
- Degrees of freedom:
  - \* Considered frequency:  $f_{min} = 200$  [MHz],  $\lambda_b = 0.75$  [m];
  - \*  $\frac{(2ka)^2}{2} = \frac{(2 \times \frac{2\pi}{\lambda_b} \times \frac{L\sqrt{2}}{2})^2}{2} = 4\pi^2 \left(\frac{L}{\lambda_b}\right)^2 = 4\pi^2 \left(\frac{0.8}{0.75}\right)^2 \simeq 44.87$ ;
- Number of cells:  $N = 49 = 7 \times 7$ ;
- Maximum number of *IMSA* steps:  $S = 4$ ;
- Side ratio threshold:  $\eta_{th} = 0.2$ ;

- ***MF – IMSA – PSO* parameters**

- Maximum number of iterations:  $I = 20000$ ;
- Swarm dimension:  $P = \frac{5}{100} \times U = 250$ ;
- $C_1 = C_2 = 2.0$ ;
- Inertial weight:  $w = 0.4$ ;
- Velocity clamping: enabled;

- ***MF – IMSA – CG* parameters**

- Maximum number of iterations:  $I = 200$ ;

**Signal to noise ratio (on  $E_{tot}(t)$ )**

- $SNR = \{50, 40, 30, 20\}$  [dB] + Noiseless data.



2.1.2  $d_{obj} = 0.16$  [m] - MF-IMSA-PSO vs. MF-IMSA-CG: Final reconstructions

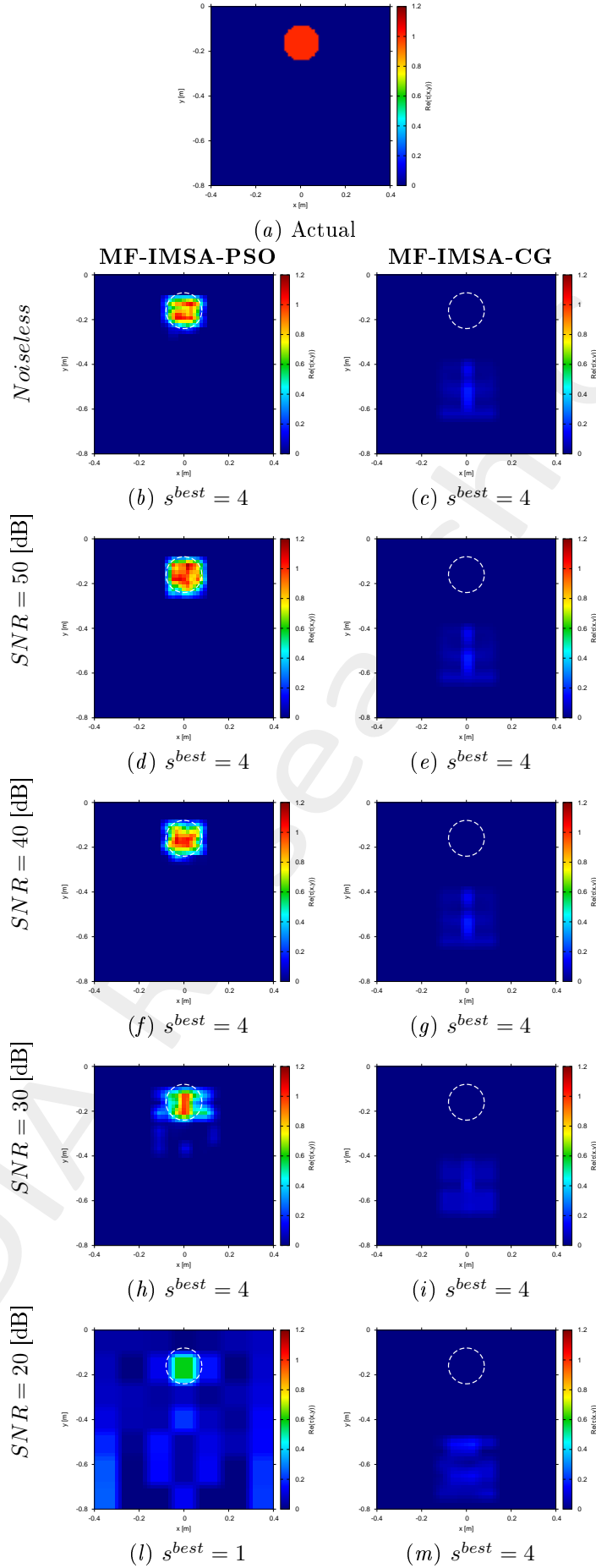


Figure 4: MF-IMSA-PSO vs. MF-IMSA-CG: Retrieved dielectric profiles at the IMSA convergence step ( $s^{best}$ ).

2.1.3  $d_{obj} = 0.4$  [m] - MF-IMSA-PSO vs. MF-IMSA-CG: Final reconstructions

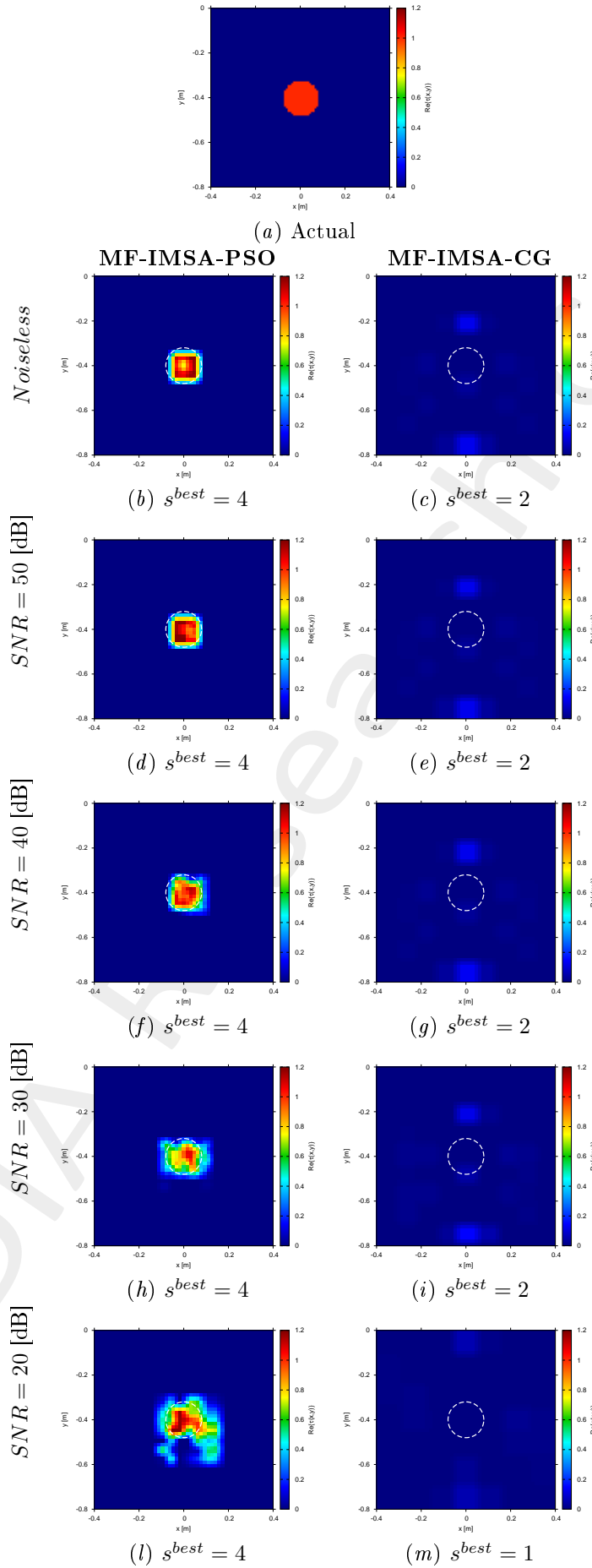


Figure 5: MF-IMSA-PSO vs. MF-IMSA-CG: Retrieved dielectric profiles at the IMSA convergence step ( $s^{best}$ ).

2.1.4  $d_{obj} = 0.64$  [m] - MF-IMSA-PSO vs. MF-IMSA-CG: Final reconstructions

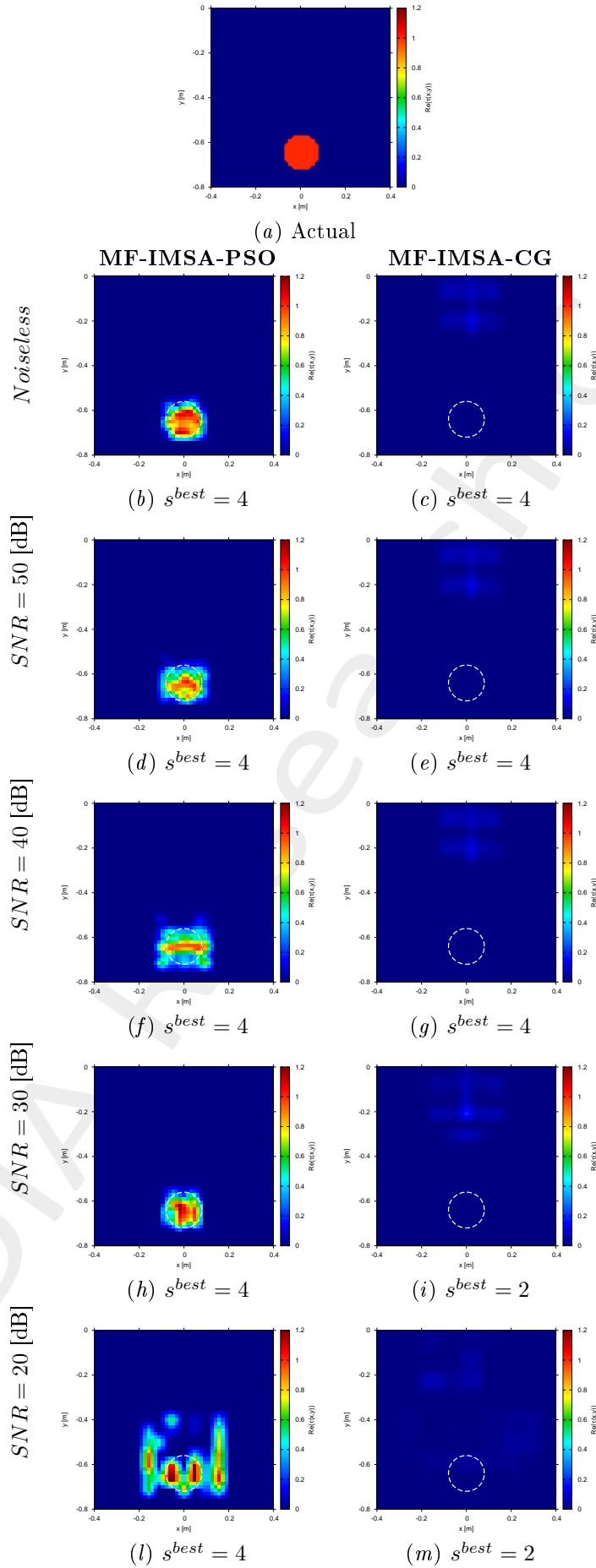


Figure 6: MF-IMSA-PSO vs. MF-IMSA-CG: Retrieved dielectric profiles at the IMSA convergence step ( $s^{best}$ ).

### 2.1.5 MF-IMSA-PSO vs. MF-IMSA-CG: Errors vs. $d_{obj}$

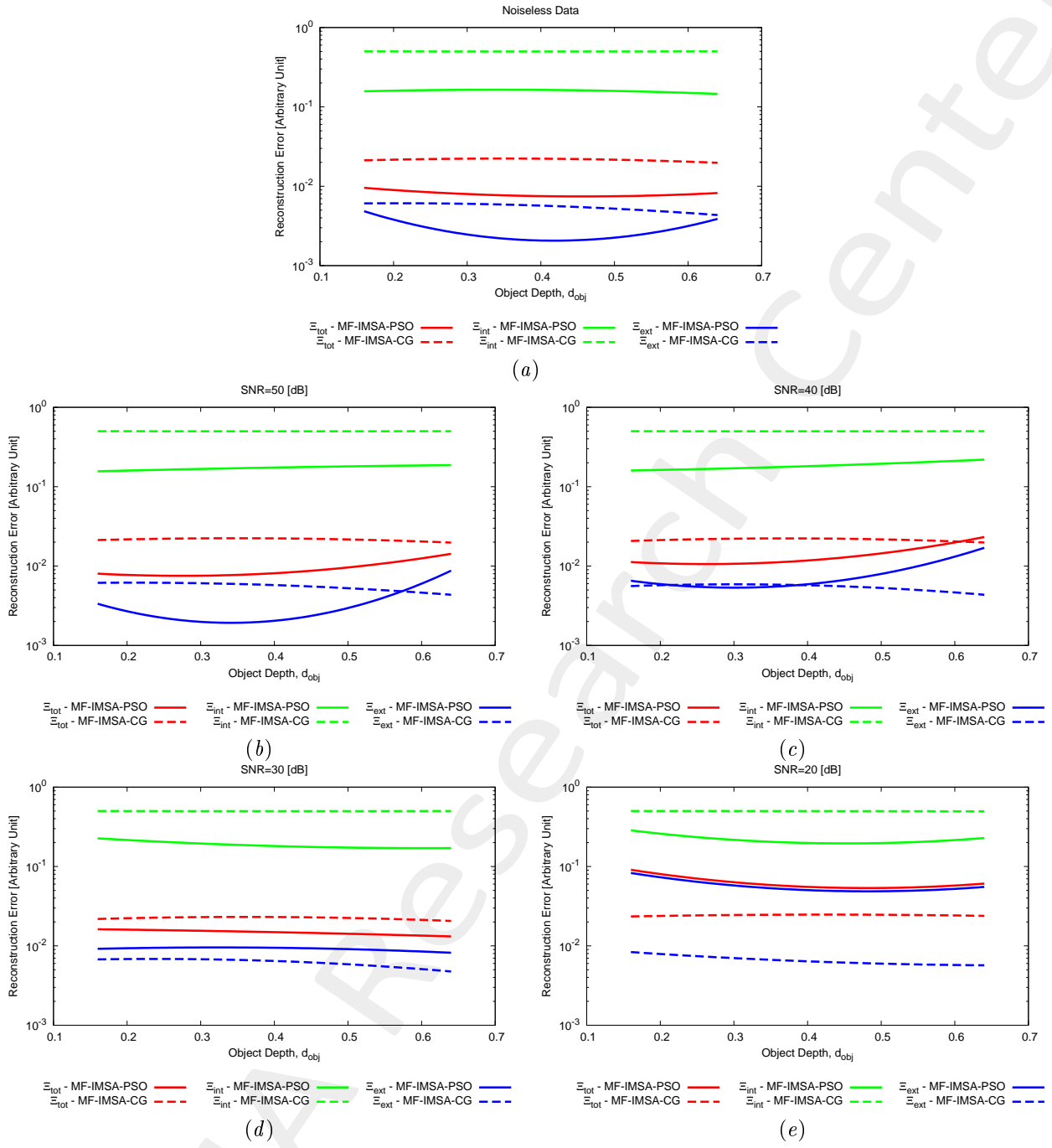


Figure 7: MF-IMSA-PSO vs. MF-IMSA-CG: Reconstruction errors vs. the object depth ( $d_{obj}$ ).

2.1.6 MF-IMSA-PSO vs. MF-IMSA-CG: Errors vs. SNR

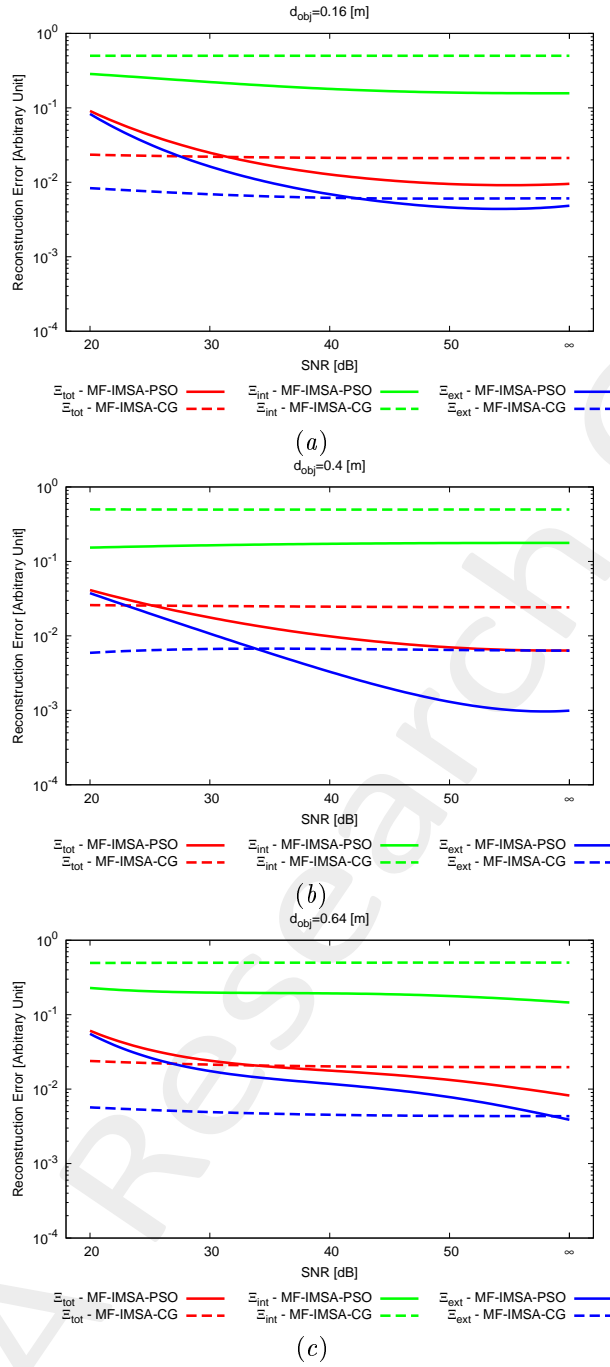


Figure 8: MF-IMSA-PSO vs. MF-IMSA-CG: Reconstruction errors vs. SNR.

## 3 Smoothly Varying Background Medium

### 3.1 Circular void ( $\varepsilon_{r,obj} = 1.0$ , $\sigma_{obj} = 0.0$ [S/m])

#### 3.1.1 Parameters

##### Background

Inhomogeneous and nonmagnetic background composed by two half spaces

- Upper half space ( $y > 0$  - air):  $\varepsilon_{ra} = 1.0$ ,  $\sigma_a = 0.0$ ;
- Lower half space ( $y < 0$  - soil):
  - Inhomogeneous background, smoothly varying
  - $\varepsilon_{rb} \in [3.5, 4.5]$ ,  $\sigma_b = 10^{-3}$ [S/m], from top (interface) to bottom;
  - Number of quantization levels for  $\varepsilon_{rb}$ :  $Q_{\varepsilon_{rb}} = 20$ ;
  - Below the bottom line of  $D_{inv}$  the relative permittivity has been set equal to the maximum value ( $\varepsilon_{rb,max} = 4.5$ );
  - Guess for the (homogeneous) background:  $\varepsilon_{rb}^{guess} = 4.0$ ,  $\sigma_b^{guess} = 10^{-3}$ [S/m];

##### Investigation domain ( $D_{inv}$ )

- Side:  $L_{D_{inv}} = 0.8$  [m];
- Barycenter:  $(x_{bar}^{D_{inv}}, y_{bar}^{D_{inv}}) = (0.00, -0.4)$  [m];

##### Time-Domain forward solver ( $FDTD - GPRMax2D$ )

- Side of the simulated domain:  $L = 6$  [m];
- Number of cells:  $N^{FDTD} = 750 \times 750 = 5.625 \times 10^5$ ;
- Side of the  $FDTD$  cells  $l^{FDTD} = 0.008$  [m];
- Simulation time window:  $T^{FDTD} = 20 \times 10^{-9}$  [sec];
- Time step:  $\Delta t^{FDTD} = 1.89 \times 10^{-11}$  [sec];
- Number of time samples:  $N_t^{FDTD} = 1060$ ;
- Boundary conditions: perfectly matched layer ( $PML$ );
- Source type: Gaussian mono-cycle (first Gaussian pulse derivative, called “Ricker” in  $GPRMax2D$ )
  - Central frequency:  $f_0 = 300$  [MHz];
  - Source amplitude:  $A = 1.0$  [A];

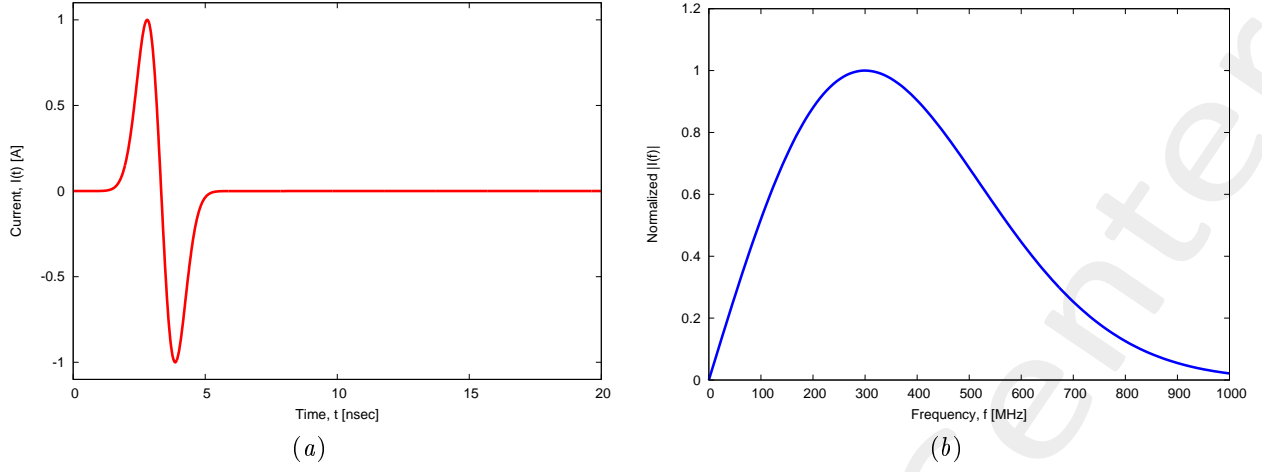


Figure 9: *GPRMax2D* excitation signal. (a) Time pulse, (b) normalized frequency spectrum.

### Frequency parameters

- Frequency range:  $f \in [f_{min}, f_{max}] = [200.0, 600.0]$  [MHz] ( $-3$  [dB] bandwidth of the Gaussian Monocycle excitation centered at  $f_0 = 300$  [MHz]);
- Frequency step:  $\Delta f = 100$  [MHz] ( $F = 5$  frequency steps in  $[f_{min}, f_{max}]$ );

$f$ [MHz]	$\lambda_a$ [m]	$\lambda_b$ [m]	$f^*$ [MHz]
200.0	1.50	0.75	200.5
300.0	1.00	0.50	297.6
400.0	0.75	0.37	401.1
500.0	0.60	0.30	498.1
600.0	0.50	0.25	601.6

Table 2: Considered frequencies and corresponding wavelength in the upper medium ( $\lambda_a$ , free space) and in the lower medium ( $\lambda_b$ , soil).  $f^*$  is the nearest frequency sample available from transformed time-domain data, and represents the real frequency considered by the inversion algorithm.

### Scatterer

- Type: Circular void;
- Barycenter:  $(x_{obj}, y_{obj}) = (-0.16, -0.4)$  [m];
- Radius:  $r_{obj} = 0.08$  [m];
- Electromagnetic properties:  $\varepsilon_{r,obj} = 1.0$ ,  $\sigma_{obj} = 0.0$  [S/m];
- Contrast function:  $\tau = -3.0 + j0.045$  ( $@f_{cent} = 400$  [MHz]);

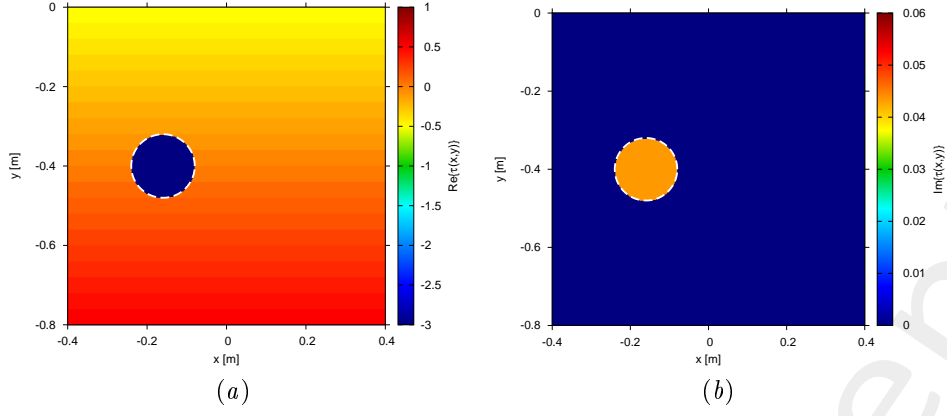


Figure 10: Actual object (a) real part and (b) imaginary part.

### Measurement setup

- Considered frequency:  $f_{min} = 200$  [MHz],  $\lambda_b = 0.75$  [m].<sup>2</sup>
- #DoFs =  $2ka = \frac{2\pi}{\lambda_b} L\sqrt{2} = \frac{2\pi}{0.75} 0.8\sqrt{2} \simeq 9.5$ ;
- Number of views (sources):  $V = 10$ ;
  - $\min\{x_v\} = -0.5$  [m],  $\max\{x_v\} = 0.5$  [m];
  - height:  $y_v = 0.1$  [m],  $\forall v = 1, \dots, V$ ;
- Number of measurement points:  $M = 9$ ;
  - $\min\{x_m\} = -0.5$  [m],  $\max\{x_m\} = 0.5$  [m];
  - height:  $y_m = 0.1$  [m],  $\forall m = 1, \dots, M$ ;

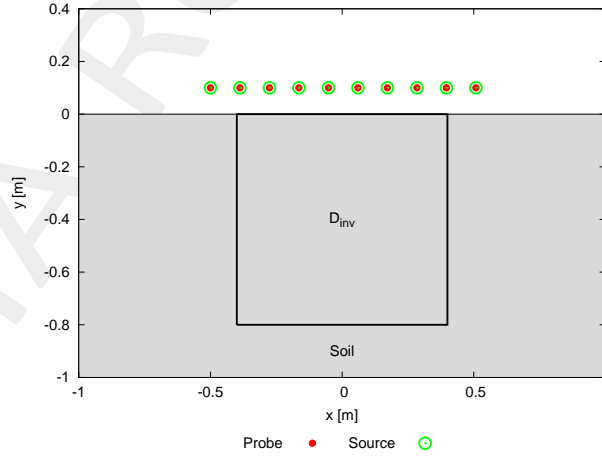


Figure 11: Location of the measurement points ( $M = 9$ ) and of the sources ( $V = 10$ ). Only one source is active for each view.

### Inverse solver parameters

- Shared parameters

<sup>2</sup>NOTE: This choice is done in order to keep the number of unknowns lower than 5000.



- Number of unknowns:  $U = 2N(1 + VF) = 4998$ ;
- Weight of the state term of the functional: 1.0;
- Weight of the data term of the functional: 1.0;
- Weight of the penalty term of the functional: 0.0;
- Convergence threshold:  $10^{-10}$ ;
- Variable ranges:
  - \*  $\varepsilon_r \in [1.0, 4.0]$ ,  $\sigma \in [0.0, 1.0 \times 10^{-3}]$  [S/m];
  - \*  $\Re\{E_{tot}^{int}\} \in [-8, 8]$ ,  $\Im\{E_{tot}^{int}\} \in [-8, 8]$ ;
- Degrees of freedom:
  - \* Considered frequency:  $f_{min} = 200$  [MHz],  $\lambda_b = 0.75$  [m];
  - \*  $\frac{(2ka)^2}{2} = \frac{(2 \times \frac{2\pi}{\lambda_b} \times \frac{L\sqrt{2}}{2})^2}{2} = 4\pi^2 \left(\frac{L}{\lambda_b}\right)^2 = 4\pi^2 \left(\frac{0.8}{0.75}\right)^2 \simeq 44.87$ ;
- Number of cells:  $N = 49 = 7 \times 7$ ;
- Maximum number of *IMSA* steps:  $S = 4$ ;
- Side ratio threshold:  $\eta_{th} = 0.2$ ;

- ***MF – IMSA – PSO* parameters**

- Maximum number of iterations:  $I = 20000$ ;
- Swarm dimension:  $P = \frac{5}{100} \times U = 250$ ;
- $C_1 = C_2 = 2.0$ ;
- Inertial weight:  $w = 0.4$ ;
- Velocity clamping: enabled;

- ***MF – IMSA – CG* parameters**

- Maximum number of iterations:  $I = 200$ ;

**Signal to noise ratio (on  $E_{tot}(t)$ )**

- $SNR = \{50, 40, 30, 20\}$  [dB] + Noiseless data.

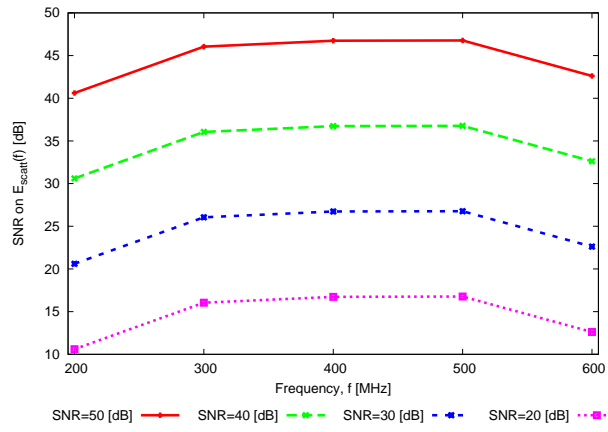


Figure 12: Signal to noise ratio ( $SNR$  [dB]) computed on the external scattered field in frequency domain for each considered frequency and for each input  $SNR$  on the measured total field in time-domain.

SNR on $E_{tot}(t)$ [dB]	Av. SNR on $E_{scatt}(f)$ [dB]
50	44.5
40	34.5
30	24.5
20	14.5

Table 3: Average  $SNR$  measured on the scattered field in frequency domain.

### 3.1.2 MF – IMSA – PSO: Final reconstructions

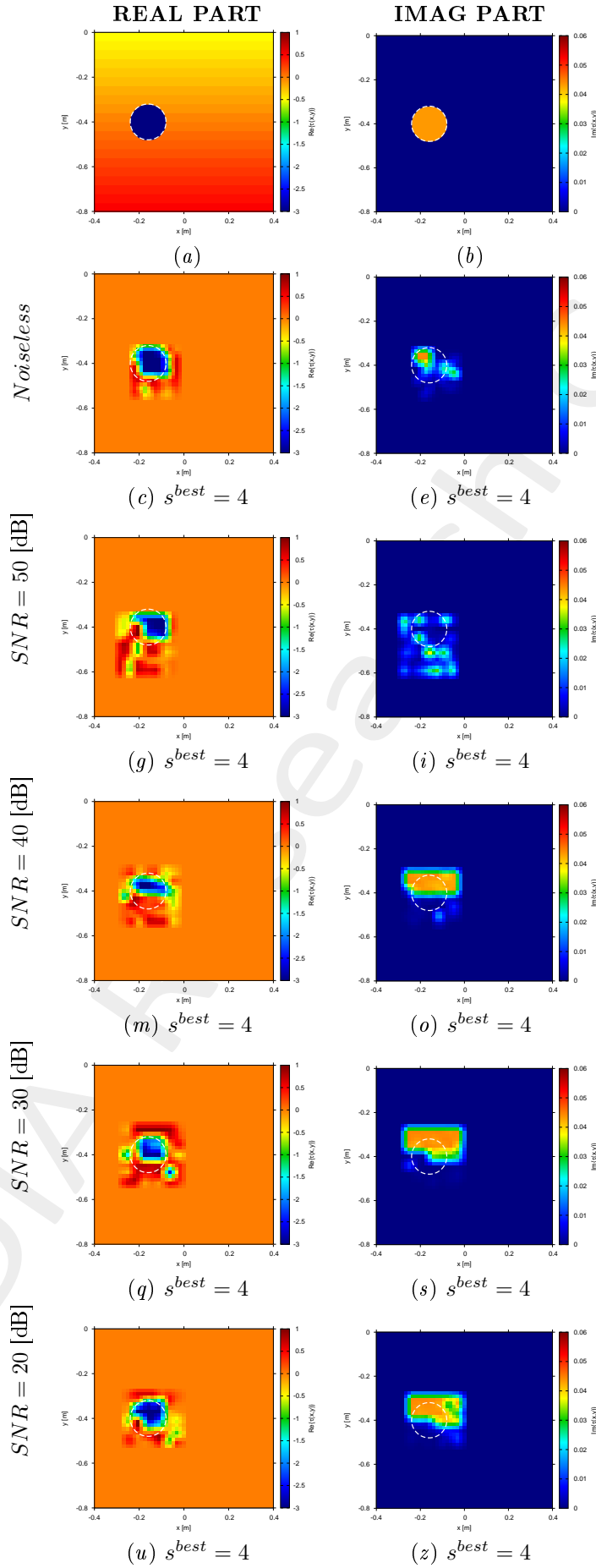


Figure 13: MF – IMSA – PSO: Retrieved dielectric profiles at the IMSA convergence step ( $s^{best}$ ).

### 3.1.3 Reconstruction errors

	$s^{best}$	$\Xi_{tot}$	$\Xi_{int}$	$\Xi_{ext}$
<i>Noiseless</i>	4	$3.45 \times 10^{-1}$	$5.34 \times 10^{-1}$	$3.39 \times 10^{-1}$
<i>SNR = 50 [dB]</i>	4	$3.64 \times 10^{-1}$	$7.20 \times 10^{-1}$	$3.53 \times 10^{-1}$
<i>SNR = 40 [dB]</i>	4	$3.74 \times 10^{-1}$	$9.70 \times 10^{-1}$	$3.55 \times 10^{-1}$
<i>SNR = 30 [dB]</i>	4	$3.91 \times 10^{-1}$	1.09	$3.69 \times 10^{-1}$
<i>SNR = 20 [dB]</i>	4	$3.68 \times 10^{-1}$	$7.85 \times 10^{-1}$	$3.55 \times 10^{-1}$

Table 4: *MF – IMSA – PSO*: Reconstruction errors at  $s^{best}$ .

## 4 Conclusions

The reported numerical validation in this document has shown that

- very accurate reconstructions of the electromagnetic characteristics of the buried investigation domain are always achieved by the  $MF - IMSA - PSO$ ;
- the  $MF - IMSA - PSO$  is able to faithfully retrieve the shape and contrast of objects buried at different depths below the interface, even when considering high levels of noise on the processed  $GPR$  radargrams. Moreover, significantly better solutions are yielded with respect to the state-of-the-art  $MF - IMSA - CG$  approach [5];
- the  $MF - IMSA - PSO$  is able to correctly retrieve unknown buried objects also when the relative permittivity of the background medium is not constant but smoothing varying within certain ranges around the nominal value.

## References

- [1] P. Rocca, M. Benedetti, M. Donelli, D. Franceschini, and A. Massa, "Evolutionary optimization as applied to inverse problems," *Inverse Probl.*, vol. 25, pp. 1-41, Dec. 2009.
- [2] P. Rocca, G. Oliveri, and A. Massa, "Differential Evolution as applied to electromagnetics," *IEEE Antennas Propag. Mag.*, vol. 53, no. 1, pp. 38-49, Feb. 2011.
- [3] M. Salucci, G. Oliveri, and A. Massa, "GPR prospecting through an inverse scattering frequency-hopping multi-focusing approach," *IEEE Trans. Geosci. Remote Sens.*, vol. 53, no. 12, pp. 6573-6592, Dec. 2015.
- [4] M. Salucci, L. Poli, and A. Massa, "Advanced multi-frequency GPR data processing for non-linear deterministic imaging," *Signal Processing - Special Issue on 'Advanced Ground-Penetrating Radar Signal-Processing Techniques,'* vol. 132, pp. 306-318, Mar. 2017.
- [5] M. Salucci, L. Poli, N. Anselmi and A. Massa, "Multifrequency particle swarm optimization for enhanced multiresolution GPR microwave imaging," *IEEE Trans. Geosci. Remote Sens.*, vol. 55, no. 3, pp. 1305-1317, Mar. 2017.
- [6] A. Massa, P. Rocca, and G. Oliveri, "Compressive sensing in electromagnetics - A review," *IEEE Antennas Propag. Mag.*, pp. 224-238, vol. 57, no. 1, Feb. 2015.
- [7] A. Massa and F. Teixeira, Guest-Editorial: Special Cluster on Compressive Sensing as Applied to Electromagnetics, *IEEE Antennas Wireless Propag. Lett.*, vol. 14, pp. 1022-1026, 2015.
- [8] N. Anselmi, G. Oliveri, M. Salucci, and A. Massa, "Wavelet-based compressive imaging of sparse targets," *IEEE Trans. Antennas Propag.*, vol. 63, no. 11, pp. 4889-4900, Nov. 2015.
- [9] G. Oliveri, N. Anselmi, and A. Massa, "Compressive sensing imaging of non-sparse 2D scatterers by a total-variation approach within the Born approximation," *IEEE Trans. Antennas Propag.*, vol. 62, no. 10, pp. 5157-5170, Oct. 2014.
- [10] T. Moriyama, G. Oliveri, M. Salucci, and T. Takenaka, "A multi-scaling forward-backward time-stepping method for microwave imaging," *IEICE Electron. Expr.*, vol. 11, no. 16, pp. 1-12, Aug. 2014.
- [11] T. Moriyama, M. Salucci, M. Tanaka, and T. Takenaka, "Image reconstruction from total electric field data with no information on the incident field," *J. Electromagnet. Wave.*, vol. 30, no. 9, pp. 1162-1170, 2016.
- [12] F. Viani, L. Poli, G. Oliveri, F. Robol, and A. Massa, "Sparse scatterers imaging through approximated multi-task compressive sensing strategies," *Microw. Opt. Technol. Lett.*, vol. 55, no. 7, pp. 1553-1557, Jul. 2013.
- [13] M. Salucci, N. Anselmi, G. Oliveri, P. Calmon, R. Miorelli, C. Reboud, and A. Massa, "Real-time NDT-NDE through an innovative adaptive partial least squares SVR inversion approach," *IEEE Trans. Geosci. Remote Sens.*, vol. 54, no. 11, pp. 6818-6832, Nov. 2016.

- [14] L. Poli, G. Oliveri, and A. Massa, "Imaging sparse metallic cylinders through a local shape function bayesian compressing sensing approach," *J. Opt. Soc. Am. A*, vol. 30, no. 6, pp. 1261-1272, Jun. 2013.
- [15] M. Donelli, D. Franceschini, P. Rocca, and A. Massa, "Three-dimensional microwave imaging problems solved through an efficient multiscaling particle swarm optimization," *IEEE Trans. Geosci. Remote Sensing*, vol. 47, no. 5, pp. 1467-1481, May 2009.